

# Bistatic Synthetic Aperture Radar Imaging: Theory, Simulations, and Validations

Fabrice Comblet, Ali Khenchaf, *Member, IEEE*, Alexandre Baussard, and Fabrice Pellen

**Abstract**—A three-dimensional “full-polarized” model for arbitrary transmitter, receiver and target motions in bistatic synthetic aperture radar configurations is proposed. Qualitative validation of this model is presented through comparison with existing results and quantitative validation is obtained from proposed general analytical resolution equations. To take into account complex targets, geometric theory of diffraction based models are considered. Some numerical results are proposed in bistatic and monostatic configurations which permit to check the performance of the proposed model and to highlight the interest of the bistatic synthetic aperture radar imaging.

**Index Terms**—Bistatic synthetic aperture radar, complex objects, simulations, vectorial model.

## I. INTRODUCTION

SYNTHETIC APERTURE RADAR (SAR) imaging has several advantages in comparison with other techniques like, for example, optical imaging since electromagnetic waves are not very sensitive to darkness, clouds, etc. At the present time, the most used configuration is the monostatic one (i.e., transmitter and receiver are the same antenna) which is easily operational due to the fact that it needs only a single platform operating as transmitter and receiver. However, stealth radar targets multiplication and the need for more accurate observations imply new radar imaging configurations and processing developments.

Bistatic configurations should overcome the monostatic limitations. Basically, bistatic radars operate with separated transmitting and receiving antennas where each platform assume different velocities and different flight paths [Fig. 1(a)] so their detection and localization are more difficult. If these systems offer some degrees of freedom, they are also more complex to implement than monostatic ones [8]. However, the potential of bistatic measurements motivates the actual studies. Bistatic SAR images include informations which complete monostatic images due to different scattering mechanisms involved. New models and techniques in bistatic and multistatic SAR systems increase the possibilities for civil or military applications.

In [8] one can find an overview of bistatic and multistatic radar systems and in [7] an history of the bistatic radar cross

section (RCS). During the last years, the interest for bistatic configurations increased. Many researches have been focused into bistatic RCS, like for example in [5], [9], and other into bistatic radar imaging [3], [4], [12], [13], [16].

In this paper a three-dimensional (3-D) vectorial model for general bistatic synthetic aperture radar constellations made of moving transmitter, receiver and target is investigated. The bistatic SAR images are obtained using a bistatic range doppler algorithm (RDA) applied on the (polarized) electromagnetic field detected by the receiver. The resulting images are qualitatively compared with results already published in the literature [16], [17], and quantitatively validated from proposed general analytical resolution equations.

To model the response of canonical scattering objects, the geometric theory of diffraction (GTD) [11] can be used. Then, taking advantage of [14], canonical scattering center models are considered in order to model complex targets. From these complex objects, the monostatic and the bistatic configurations are compared.

The paper is organized as follows. Section II introduces the bistatic vectorial model, the imaging problem, and presents some numerical results. In Section III, the proposed model is quantitatively validated from the computation of the theoretical resolutions. Section IV shows some results from complex objects. Finally, Section V gives some concluding remarks.

## II. BISTATIC SAR IMAGING

### A. Bistatic Model

The computation of the simulated signal for a bistatic configuration in the general case [see Fig. 1(a)], where the transmitter ( $T$ ), the target ( $P$ ) and the receiver ( $R$ ) are moving, is presented in [1].

The polarized signal radiated by an antenna is written in a vectorial formulation as

$$\vec{E}_i(t) = E_0 s_e(t) [G_T] \vec{q}_T \quad (1)$$

where  $E_0$  is the electromagnetic field amplitude,  $s_e(t)$  the transmitted waveform,  $[G_T]$  the transmitting radiation pattern matrix and  $\vec{q}_T$  the transmitting Jones vector which depends on the transmitting antenna polarization. The choice of the transmitted signal has a strong influence on the detection capabilities of the radar. Using chirp (linear frequency modulation) allows to fine range resolutions and to improve detection performances. In this case, the frequency is a linear swept from  $f_0 - \Delta f/2$  to  $f_0 + \Delta f/2$ . The time variation of the frequency depends on

Manuscript received May 3, 2005; revised May 19, 2006.

F. Comblet, A. Khenchaf, and A. Baussard are with E<sup>3</sup>I<sup>2</sup> Laboratory (EA3876)-ENSIETA, 29806 Brest, Cedex 9-France (e-mail: fabrice.comblet@ensieta.fr; ali.khenchaf@ensieta.fr; alexandre.baussard@ensieta.fr).

F. Pellen is with the LSOL Laboratory (EA938), 29238 Brest, Cedex 3-France (e-mail: Fabrice.Pellen@univ-brest.fr).

Color versions of Figs. 6, 8, and 9 are available online at <http://ieeexplore.ieee.org>.

Digital Object Identifier 10.1109/TAP.2006.884223

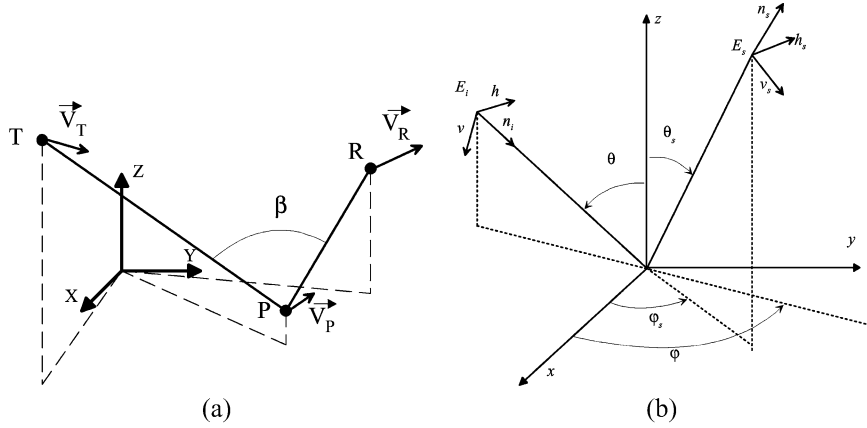


Fig. 1. General bistatic configuration. (a) Geometrical bistatic configuration. (b) Polarimetric bistatic configuration.

the carrier frequency  $f_0$ , the transmitted bandwidth  $\Delta f$  and the pulse duration  $\tau$

$$f(t) = f_0 + \frac{\Delta f}{\tau}t, \text{ with } |t| \leq \frac{\tau}{2}. \quad (2)$$

The transmitted waveform is given by

$$s_e(t) = \Pi_{[-\tau/2, \tau/2]}(t) A e^{2\pi j(f_0 t + \frac{\Delta f}{2\tau} t^2)} \quad (3)$$

where  $A$  denotes the amplitude and  $j$  stands for the complex number.  $\Pi_{[-\tau/2, \tau/2]}(t)$  is the rectangular function; that is  $\Pi_{[-\tau/2, \tau/2]}(t)$  equal 1 if  $|t| \leq (\tau/2)$  and 0 elsewhere.

The polarization of the electromagnetic plane wave scattered by a target is generally different from the incident wave. This polarization change depends on the target characteristics which are brought into the coherent scattering matrix  $[S]$ . Let  $\vec{E}_i$  and  $\vec{E}_s$  be, respectively, the Jones vectors of the transmitted and received electromagnetic wave (see Fig. 1(b)). Using an orthogonal linear  $(v, h)$  polarization basis, the relation between the received and the transmitted electromagnetic field is given, in the  $(v_s, h_s)$  basis, by

$$\vec{E}_s(t) = [S] \vec{E}_i(t) = \begin{bmatrix} a_{v_s v} & a_{v_s h} \\ a_{h_s v} & a_{h_s h} \end{bmatrix} \vec{E}_i(t). \quad (4)$$

The coefficients  $a_{pq}$  of the scattering matrix  $[S]$  depend on the geometrical and physical features of the target. They are also function of the target observation angles and of the transmitted wave frequency.

Note that in SAR imaging, when the carrier frequency is in the X-band, the bandwidth is less than 100 MHz and the pulse width is about 40  $\mu$ s. So, one can consider that the antenna radiation pattern and the scattering characteristics of the target are constant during one acquisition.

In a bistatic radiolink, the distances between the transmitter, the target and the receiver change during time, depending on their velocities  $\vec{V}_T(t)$ ,  $\vec{V}_P(t)$ , and  $\vec{V}_R(t)$ , respectively.

In what follows, one assumes that the velocity of each component is constant between the transmitting time  $t$  and the receiving time  $t + \delta t_{TR}(t)$ , where  $\delta t_{TR}(t)$  denotes the transmitter-

receiver propagation delay. In the bistatic configuration  $\delta t_{TR}(t)$  is the sum of  $\delta t_{TP}(t)$  and  $\delta t_{PR}(t)$ , which are respectively the transmitter-target and target-receiver propagation delay. See [1] for detailed expressions of the propagation delays.

From [1], the general expression of the received signal is given by

$$\begin{aligned} s_r(t) &= \Pi_{[-\tau/2, \tau/2]}(t - \delta t_{TR}(t)) \kappa s_e(t - \delta t_{TR}(t)) \\ &= \Pi_{[-\tau/2, \tau/2]}(t - \delta t_{TR}(t)) \\ &\quad \times \kappa A e^{2\pi j(f_0(t - \delta t_{TR}(t)) + \frac{\Delta f}{2\tau}(t - \delta t_{TR}(t))^2)}. \end{aligned} \quad (5)$$

where  $|t - \delta t_{TR}(t)| \leq \tau/2$  and  $\kappa$  depends on the transmitting antenna radiation, the scattering matrix, the receiving antenna radiation.  $\kappa$  is given by

$$\kappa = \frac{E_0}{c^2 \delta t_{TP}(t) \delta t_{PR}(t)} \vec{q}_R^T [G_R]^T [Q_R]^T [S^{FSA}] [Q_T] [G_T] \vec{q}_T \quad (6)$$

where  $\vec{q}_R$  is the receiving Jones vector,  $[G_R]^T$  is the transposed receiving antenna radiation pattern matrix,  $[Q_R]$  is the linking matrices between the base associated to the receiving antenna and the base associated to the electromagnetic field propagation and  $[Q_T]$  is the linking matrices between the base associated to the transmitting antenna and the base associated to the electromagnetic field propagation.  $[S^{FSA}]$  denotes the scattering matrix in the forward scattering alignment convention.

The proposed model is particularly interesting because the electromagnetic field propagation is considered in a three-dimensional way which allows to take into account propagation, shadow or masked effects. Whereas other simulator take only into account the amplitude and phase of each reflectors on the observed scene. Moreover, in contrast with most of actual SAR simulators based on scalar field, this model uses a “full-polarized” configuration.

## B. Bistatic SAR Processing

In synthetic aperture, we need to discriminate short time (for the duration of an acquisition) and long time (for the duration of the aperture). Let  $t_a$  be the short time, so  $-\tau/2 \leq t_a < T_a - \tau/2$  where  $T_a$  is the time duration of an acquisition. Let

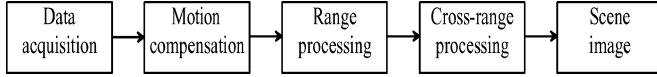


Fig. 2. Bistatic SAR processing chain.

$nT_a$  be the long time, with  $0 \leq n \leq N$  where  $N$  is the total number of acquisitions. Then the transmitted waveform for the  $n^{th}$  acquisition is given by

$$s_e(t_a, n) = \Pi_{[-\tau/2, \tau/2]}(t_a + nT_a) \times A e^{2\pi j(f_0(t_a + nT_a) + \frac{\Delta f}{2\tau}(t_a + nT_a)^2)} \quad (7)$$

and the received signal is given by

$$s_r(t_a, n) = \Pi_{[-\tau/2, \tau/2]}(t_a + nT_a - \delta t_{TR,n}) \times \kappa A e^{2\pi j(f_0(t_a + nT_a - \delta t_{TR,n}) + \frac{\Delta f}{2\tau}(t_a + nT_a - \delta t_{TR,n})^2)}. \quad (8)$$

In this equation, and in what follows,  $\delta t_{TR,n}$  stands for  $\delta t_{TR,n}(t_a)$ .

From this signal, the image is obtained by using an RDA method [16] adapted to the considered bistatic configuration (see Fig. 2). This method can be splitted into the following three steps.

1) *Motion Compensation*: The first stage of the RDA is the motion compensation. The corrected signal  $s_1(t_a, n)$  is obtained by a multiplication, in the frequency domain, of each acquisition by  $e^{-2\pi j(\delta D_{T,n} + \delta D_{R,n})t}$ , where  $\delta D_{T,n}$  and  $\delta D_{R,n}$  correspond respectively to the transmitter-target and the target-receiver distance variations.

2) *Range Processing*: Since the emitted signal is considered wide-band, a matched filtering using the emitted signal  $s_e(t_a, n)$  is carried out on each acquisition in order to improve the range resolution. The compressed signal  $s_c(t_a, n)$  is defined as

$$s_c(t_a, n) = \int_{-\infty}^{+\infty} s_e^*(t' - t_a, n) s_1(t', n) dt' \quad (9)$$

where  $s_e^*$  denotes the conjugate of  $s_e$ . Using (7) and (8), the compressed signal is given by

$$s_c(t_a, n) = \kappa A^2 e^{2\pi j f_0(t_a - \delta t_{TR,n})} (\tau - |t_a - \delta t_{TR,n}|) \times \text{sinc}(u(\tau - |t_a - \delta t_{TR,n}|)) \quad (10)$$

where  $u = (\pi \Delta f / \tau)(t_a - \delta t_{TR,n})$ .

Note that with the classical radar parameters,  $\tau - |t_a - \delta t_{TR,n}|$  can be approximate by  $\tau$ . Then, the compressed signal can be expressed as

$$\bar{s}_c(t_a, n) \simeq \kappa A^2 \tau e^{2\pi j f_0(t_a - \delta t_{TR,n})} \text{sinc}(\pi \Delta f(t_a - \delta t_{TR,n})). \quad (11)$$

3) *Cross-Range Processing*: Finally, the Doppler shift caused by the transmitter and the receiver motions is used in order to improve the cross-range resolution. In (11), the shift is more important in the phase term so the signal used for the cross-range processing is

$$\tilde{s}_c(t_a, n) = K e^{2\pi j f_0(t_a - \delta t_{TR,n})}. \quad (12)$$

where  $K = \kappa A^2 \tau \text{sinc}(\pi \Delta f(t_a - \delta t_{TR,n}))$ .

The transmitter-receiver propagation delay expression is  $\delta t_{TR,n} = \delta t_{TP,n} + \delta t_{PR,n}$ . The transmitter/receiver-target propagation delays can be expressed from the transmitter/receiver-target distances and the distances along the transmitter/receiver motions as

$$\begin{aligned} \delta t_{TP,n} &\simeq \frac{D_T}{c} + \frac{(nV_T T_a)^2}{2cD_T} \\ \delta t_{PR,n} &\simeq \frac{D_R}{c} + \frac{(nV_R T_a)^2}{2cD_R} \end{aligned} \quad (13)$$

where  $D_T$  and  $D_R$  are respectively the transmitter-target and receiver-target distances,  $V_T = \|\vec{V}_T\|$  and  $V_R = \|\vec{V}_R\|$ . So (12) becomes

$$\begin{aligned} \tilde{s}_c(t_a, n) &= K e^{2\pi j f_0(t_a - \frac{D_T + D_R}{c})} \\ &\times e^{2\pi j f_0\left(nT_a - \frac{(nV_T T_a)^2}{2cD_T} - \frac{(nV_R T_a)^2}{2cD_R}\right)}. \end{aligned} \quad (14)$$

The second term can be assimilated as a chirp, so a transverse matched filter is used in order to improve the cross-range resolution. This matched filter depends on the relative speed  $V_T$  between the transmitter and the target, and the relative speed  $V_R$  between the receiver and the target. The reconstructed image is given by

$$I(t_a, n) = \int_{-\infty}^{+\infty} s_t^*(n' - n) \tilde{s}_c(t_a, n') dn' \quad (15)$$

where the matched filter  $s_t(n)$  is given by  $s_t(n) = e^{2\pi j f_0(nT_a - ((nV_T T_a)^2 / 2cD_T) - ((nV_R T_a)^2 / 2cD_R))}$ . The expansion leads to

$$\begin{aligned} I(t_a, n) &= 2NK e^{2\pi j f_0\left(t_a + nT_a - \frac{D_T + D_R}{c} + \frac{(V_T nT_a)^2}{2cD_T} + \frac{(V_R nT_a)^2}{2cD_R}\right)} \\ &\times e^{-2\pi j f_0 N^2 \left(\frac{n(V_T T_a)^2}{2cD_T} + \frac{n(V_R T_a)^2}{2cD_R}\right)} \\ &\times \text{sinc}\left(2\pi f_0 N \left(\frac{n(V_T T_a)^2}{2cD_T} + \frac{n(V_R T_a)^2}{2cD_R}\right)\right). \end{aligned} \quad (16)$$

Note that in this paper no post-processing is applied to the obtained reconstruction in order to not damage the image resolutions. This allows to compare the resolutions obtained from the bistatic reconstructed images with the theoretical ones obtained from the proposed bistatic resolution equations (see Section III).

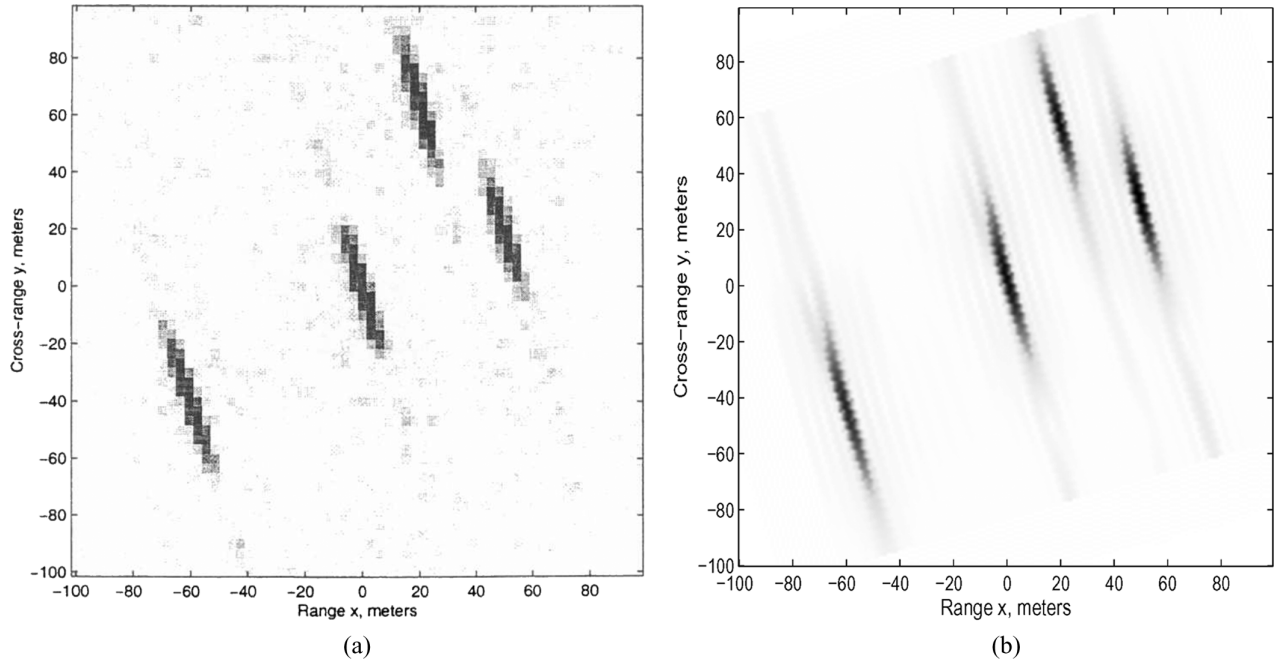


Fig. 3. Bistatic SAR images of four isotropic highlights. Comparison between Soumekh's codes and the proposed model. (a) Obtained result by Soumekh (reprinted with the permission of M. Soumekh [17]). (b) Obtained result from the proposed simulator.

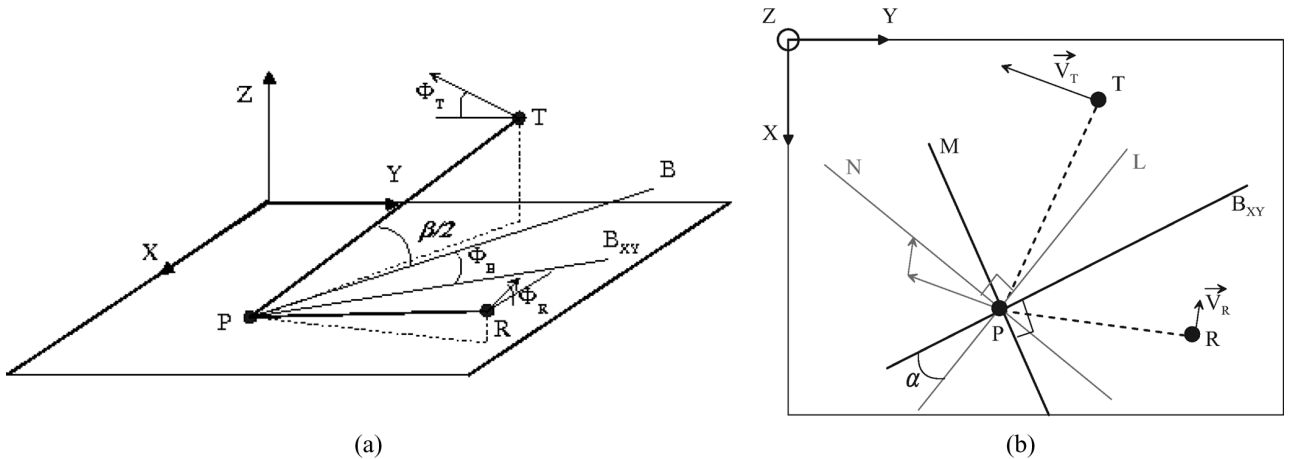


Fig. 4. Resolution directions defined in the general bistatic configuration. (a) 3-D configuration. (b) Top view of (a).

### C. Bistatic SAR Simulation

A comparison with existing results in the literature [17] is presented here for a qualitative validation of the proposed model. Fig. 3 presents simulation results obtained with the parameters proposed by Soumekh in [17]. Note that, in our model, here and in what follows, the transmitting and receiving antenna radiation patterns are considered to be isotropic.

The configuration is made of a stationary transmitter located at (3000, 2000)m, a moving receiver located at (1000,0)m which generates a 100 m aperture along the  $Y$ -direction and four isotropic highlights located at  $(-60, -40)$ m,  $(0, 0)$ m,  $(20, 60)$ m and  $(50, 20)$ m. The emitted signal is within the frequency band [80, 120] MHz.

Our simulator allows to find the position of each highlights, and the obtained results from Soumekh's codes and from our simulator are close (see Fig. 3). The differences come from the

image reconstruction methods: backprojection on sub-areas for Soumekh and bistatic RDA in our case. Moreover, Soumekh uses Hamming windows in order to reduce secondary lobes which leads to damage the resolution.

### III. BISTATIC SAR RESOLUTION

In this section, the analytical expressions of the bistatic SAR resolutions are derived for a quantitative validation of the proposed processing. Fig. 4(a) gives the general setup of the bistatic configuration.  $T$ ,  $P$  and  $R$  denote, respectively, the transmitter, the target, and the receiver.  $\beta$  is the bistatic angle,  $B$  is the bistatic bisector and  $B_{XY}$  its projection on the  $XY$ -plane. Fig. 4(b) is Fig. 4(a) top view showing the range (gray) and cross-range (black) resolution directions.

The range resolution is expressed in the  $L$ -direction which is the line perpendicular to the line  $N$  built from the sum of the

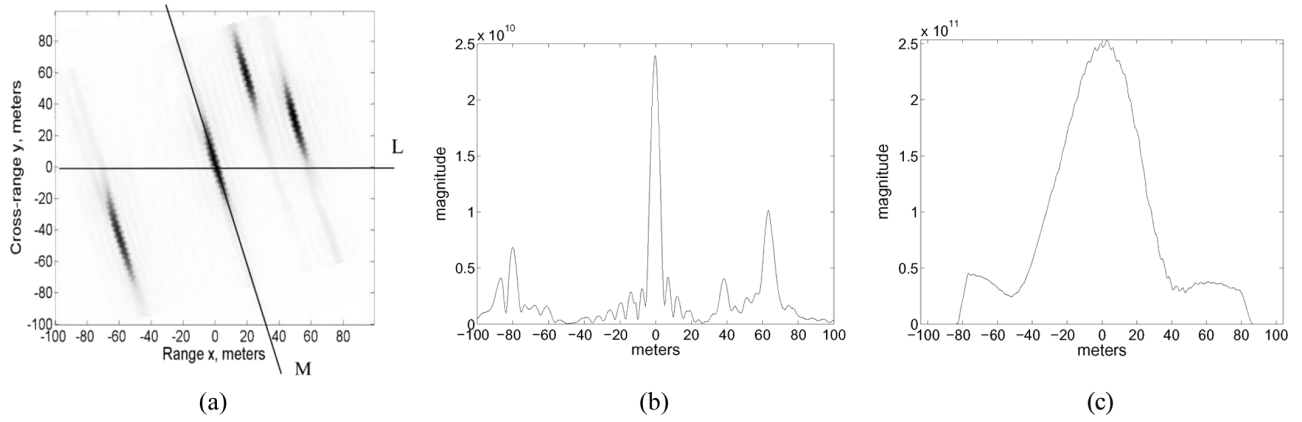


Fig. 5. Resolution values from a bistatic SAR image. (a) Obtained bistatic image of 4 highlights. (b) Magnitude evolution along the  $L$ -direction. (c) Magnitude evolution along the  $M$ -direction.

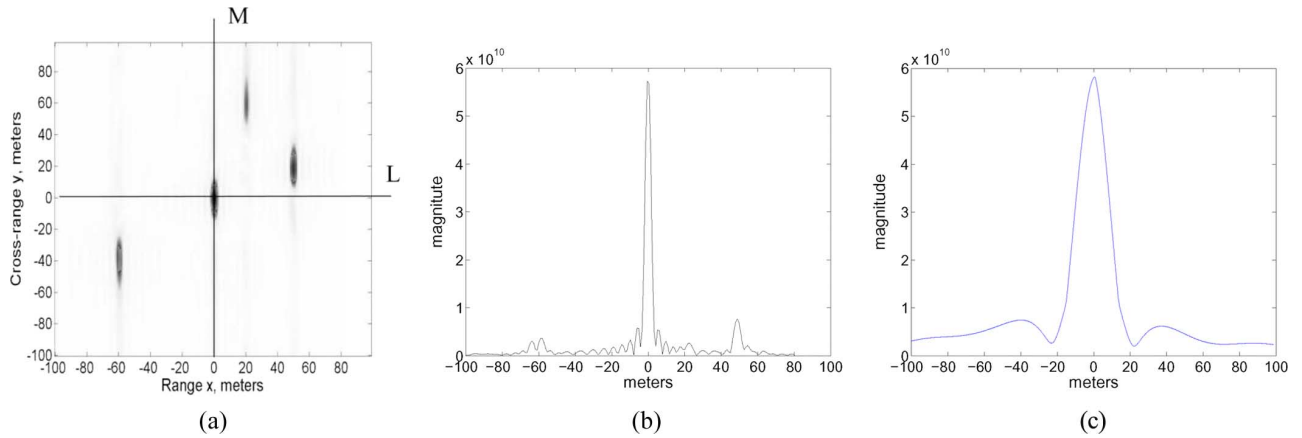


Fig. 6. Resolution values from a monostatic SAR image. (a) Monostatic image of 4 highlights. (b) Magnitude evolution along the  $L$ -direction. (c) Magnitude evolution along the  $M$ -direction.

transmitter and the receiver motion [see Fig. 4(b)]. The range resolution at  $-3.92$  dB is deduce from the sinc function of (11) and it is given by

$$\Delta R(L) = \frac{c}{2\Delta f \cos(\beta/2) \cos \alpha \cos \Phi_B} \quad (17)$$

where  $c$  is the celerity,  $\Delta f$  is the frequency bandwidth,  $\alpha$  the angle between  $L$  and  $B_{XY}$ .

The cross-range resolution is defined, from the cardinal sine of (16) at  $-3.92$  dB, in the  $M$ -direction perpendicular to  $B_{XY}$  [see Fig. 4(b)] as follows:

$$\Delta CR(M) = \frac{\lambda}{2NT_a \cos \alpha} \left( \frac{V_T \cos \Phi_T}{V_T \cos \Phi_T + V_R \cos \Phi_R} \times \frac{V_T \cos \Phi_T}{D_T} + \frac{V_R \cos \Phi_R}{V_T \cos \Phi_T + V_R \cos \Phi_R} \frac{V_R \cos \Phi_R}{D_R} \right)^{-1} \quad (18)$$

where  $\lambda$  is the wavelength,  $\gamma_{TR}$  and  $\gamma_R$  are respectively the angle subtended by the transmitter and the receiver synthetic aperture.

In (17) and (18),  $\Phi_B$ ,  $\Phi_{TR}$  and  $\Phi_R$  correspond to projection angles [see Fig. 4(a)].

From these general (17) and (18), the monostatic resolutions ( $\beta = 0^\circ$  and  $\Phi_{TR} = \Phi_R$ ) [16], the resolutions in particular bistatic configurations [10], [18] and equivalent expressions [19] can be recovered.

From (17) and (18), the theoretical bistatic resolutions of the considered setup are

$$\Delta R_{th}(L) = 7.06 \text{ m and } \Delta CR_{th}(M) = 54.13 \text{ m.}$$

From Fig. 5, the obtained resolutions are

$$\Delta R_{simu}(L) = 7 \text{ m and } \Delta CR_{simu}(M) = 54.2 \text{ m}$$

which are close to the theoretical ones.

If the same scene is now observed in the monostatic configuration, i.e., transmitter and receiver are located at (1000, 0)m and generate a 100 m aperture along the  $Y$ -direction, then the theoretical resolutions are

$$\Delta R_{th}(L) = 3.8 \text{ m and } \Delta CR_{th}(M) = 15 \text{ m}$$

and the simulated ones are (Fig. 6)

$$\Delta R_{simu}(L) = 4 \text{ m and } \Delta CR_{simu}(M) = 15 \text{ m.}$$

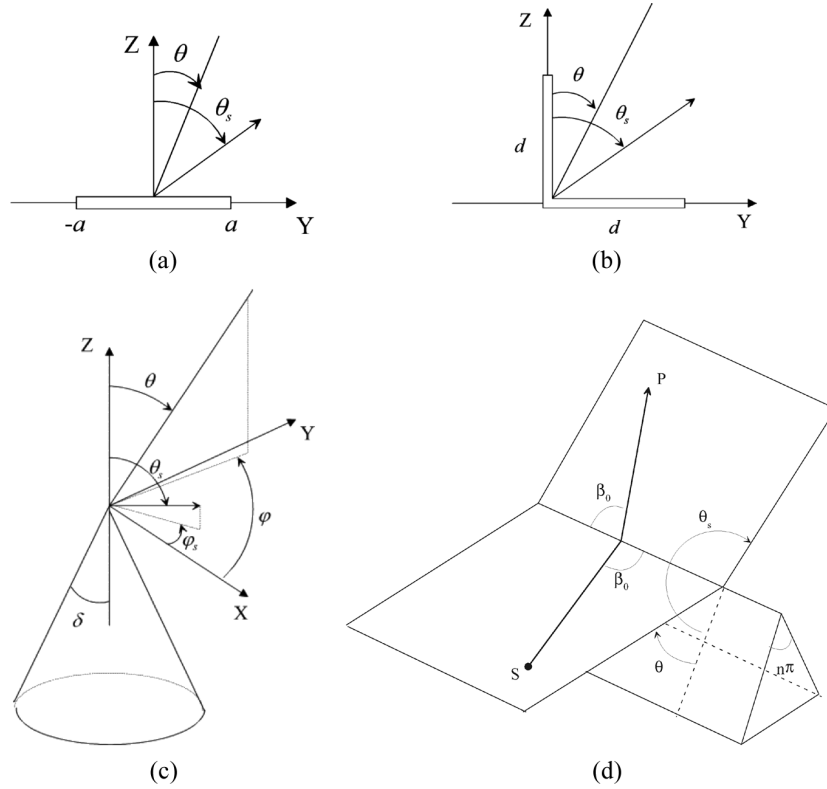


Fig. 7. Geometrical characteristics of incident and reflected electromagnetic field for canonical scattering centers. (a) Infinite strip. (b) Right angle. (c) Semi-infinite cone. (d) Discontinuity.

Here, monostatic resolutions are better than bistatic ones due to the fact that the aperture is generated simultaneously by the transmitter and the receiver, whereas the aperture in bistatic configuration is only obtained from the receiver. Moreover, in the monostatic configuration  $\beta = 0^\circ$ . This can be easily compensate by multistatic configurations and data fusion [12].

#### IV. COMPLEX TARGET IMAGING BASED ON GTD MODELS

In the first part of this section, GTD models for canonical scattering centers are reviewed. GTD-based models have been developed by Keller [11] in order to complete the geometrical optics model by introducing diffractions phenomena. The diffraction coefficients are asymptotically evaluated from scattering field diffraction integral. According to the GTD-based models, the high-frequency scattering response from a complex object is well-modeled by the sum of responses from individual scattering mechanisms.

In what follows, some canonical scattering center models (infinite strips, right angle and semi-infinite cones) proposed in [14] for bistatic RCS modeling are presented. The combination of these scattering mechanisms leads to the response of three-dimensional complex targets modeled from (approximated from) these canonical objects.

Note that for the proposed results the multipath are not taken into account. In future works this point should be enhanced.

##### A. Canonical Scattering Center Models Review

1) *Infinite Strip*: The considered canonical scattering center is made of an infinite (along the  $X$ -axis) perfectly conducting

strip of width  $2a$  along the  $Y$ -axis [see Fig. 7(a)]. One denotes  $\theta$  as the incident plane wave angle, and  $\theta_s$  as the scattered wave angle.

In the high-frequencies case, when  $k_0 a \gg 1$  (where  $k_0$  is the wave number), an approximated bistatic radar cross section is given in [15] by using Sommerfeld–MacDonald technique as

$$\begin{aligned} a_{strip,hsh}(\theta, \theta_s, a) &= \frac{1}{k_0} |A_2(\theta)A_2(\theta_s)C_1(\theta, \theta_s) \exp[jk_0 a(\sin \theta + \sin \theta_s)] \\ &\quad \mp A_1(\theta)A_1(\theta_s)C_2(\theta, \theta_s) \\ &\quad \times \exp[-jk_0 a(\sin \theta + \sin \theta_s)]|^2 \end{aligned} \quad (19)$$

$$\begin{aligned} a_{strip,vsh}(\theta, \theta_s, a) &= \frac{1}{k_0} |B_2(\theta)B_2(\theta_s)C_2(\theta, \theta_s) \exp[jk_0 a(\sin \theta + \sin \theta_s)] \\ &\quad \mp B_1(\theta)B_1(\theta_s)C_1(\theta, \theta_s) \\ &\quad \times \exp[-jk_0 a(\sin \theta + \sin \theta_s)]|^2 \end{aligned} \quad (20)$$

and

$$a_{strip,hsv} = a_{strip,vsh} = 0 \quad (21)$$

where the upper sign is used if  $|\theta_s| \geq \pi/2$ , and the lower one if  $|\theta_s| \leq \pi/2$ . The other parameters are defined as

$$A_i(\theta) = \sqrt{2} \exp(-j\pi/4) [D(\zeta_i) + jS(\zeta_i)] \quad (22)$$

$$B_i(\theta) = A_i(\theta) + \frac{j}{2\sqrt{\pi k_0 a}} \times \frac{\exp[j2k_0 a(1 \pm \sin \theta) - j(\pi/4)]}{|\cos[(\pi/4) \mp (\theta/2)]|} \quad (23)$$

$$C_i(\theta, \theta_s) = \left[ \frac{\sin[(\theta + \theta_s)/2] \pm \cos[(\theta - \theta_s)/2]}{\sin \theta + \sin \theta_s} \right] \quad (24)$$

and

$$\zeta_i = 2\sqrt{\frac{2k_0 a}{\pi} \left| \cos\left(\frac{\pi}{4} \mp \frac{\theta}{2}\right) \right|} \quad (25)$$

where the index  $i = 1$  or  $2$ , the upper sign goes with index  $i = 1$ , and the lower one with index  $i = 2$ . The functions  $D(\zeta_i)$  and  $S(\zeta_i)$  in (22) are the Fresnel integrals defined by

$$D(\zeta_i) = \int_0^{\zeta_i} \cos\left(\frac{\pi}{2} t^2\right) dt \quad (26)$$

and

$$S(\zeta_i) = \int_0^{\zeta_i} \sin\left(\frac{\pi}{2} t^2\right) dt. \quad (27)$$

2) *Right Angle*: The scattering from a right angle reflector [Fig. 7(b)], with square sides of length  $d$ , is now considered. It should be noted that in the plane or perpendicular plane of the incident wave, the scattered field is not depolarized. Akhter, in [2], showed that, providing  $\theta - \theta_s$  small, the main bistatic response of a right angle reflector is given by

$$\begin{aligned} a_{right,hs}(\theta, \theta_s, d) &= a_{right,vs}(\theta, \theta_s, d) \\ &= \sqrt{j} \sin\left(\frac{\theta + \theta_s}{2}\right) \\ &\times \text{sinc}\left[2k_0 d \sin\left(\frac{\theta + \theta_s}{2}\right) \sin\left(\frac{\theta - \theta_s}{2}\right)\right] \end{aligned} \quad (28)$$

and

$$a_{right,vs}(\theta, \theta_s, d) = a_{right,hs}(\theta, \theta_s, d) = 0 \quad (29)$$

The peak response of (28) is observed when the transmitter and receiver are at the same angle.

3) *Semi-Infinite Cone*: The bistatic radar cross section of a perfectly conducting semi-infinite circular cone [see Fig. 7(c)] is given by [6]

$$\begin{aligned} a_{cone,hs}(\theta, \theta_s) &= \frac{\sqrt{j}}{\log(\sin^2(\delta/2))} \frac{\tan(\theta/2) \tan(\theta_s/2)}{\cos \theta + \cos \theta_s}, \end{aligned} \quad (30)$$

$$\begin{aligned} a_{cone,vs}(\theta, \varphi, \theta_s, \varphi_s) &= \frac{-2\sqrt{j} \sin^2(\delta/2)}{(\cos \theta + \cos \theta_s)^3} \\ &\times [\sin \theta \sin \theta_s + 2 \cos(\varphi - \varphi_s)(1 + \cos \theta \cos \theta_s)] \end{aligned} \quad (31)$$

and

$$\begin{aligned} a_{cone,vs}(\theta, \varphi, \theta_s, \varphi_s) &= -a_{cone,hs}(\theta, \varphi, \theta_s, \varphi_s) \\ &= \frac{4\sqrt{j} \sin^2(\delta/2) \sin(\varphi - \varphi_s)}{(\cos \theta + \cos \theta_s)^2} \end{aligned} \quad (32)$$

where  $(\theta, \varphi)$  and  $(\theta_s, \varphi_s)$  are respectively incidents and reflects Euler angles and  $\delta$  the cone angle.

4) *Discontinuity*: For this last model presented in Fig. 7(d) the coefficients of the scattering matrix (see [15]) are defined as

$$\begin{aligned} a_{wedge,vs}(\theta, \theta_s, \beta_0) &= \frac{e^{-j\pi/4} \sin \frac{\pi}{n}}{n\sqrt{2k\pi} \sin \beta_0} \left\{ \frac{1}{\cos \frac{\pi}{n} - \cos \frac{\theta_s - \theta}{n}} - \frac{1}{\cos \frac{\pi}{n} - \cos \frac{\theta_s + \theta}{n}} \right\} \end{aligned} \quad (33)$$

$$\begin{aligned} a_{wedge,hs}(\theta, \theta_s, \beta_0) &= \frac{e^{-j\pi/4} \sin \frac{\pi}{n}}{n\sqrt{2k\pi} \sin \beta_0} \left\{ \frac{1}{\cos \frac{\pi}{n} - \cos \frac{\theta_s - \theta}{n}} + \frac{1}{\cos \frac{\pi}{n} - \cos \frac{\theta_s + \theta}{n}} \right\} \end{aligned} \quad (34)$$

and

$$a_{wedge,vs}(\theta, \theta_s, d) = a_{wedge,hs}(\theta, \theta_s, d) = 0. \quad (35)$$

These expressions are not useful next the singularities of the considered canonical object.

## B. Bistatic RCS of a Dihedral-Shaped Target

This target is particularly interesting due to the fact that it models the link between building and ground in urban area. Considering the dihedral at Fig. 8, the bistatic radar cross section is obtained from infinite strip and right angle characteristics

$$\begin{aligned} S_{dihedral}(\theta, \varphi, \theta_s, \varphi_s, L_m, d_m) &= S_{strip}(\varphi, \varphi_s, L_m) S_{right}(\theta, \theta_s, d_m) \end{aligned} \quad (36)$$

where  $L_m$  is the length of the dihedral, and  $d_m$  is equal to the height and depth of its sides.

For  $L_m = 10$  m,  $d_m = 5$  m,  $\theta = 30^\circ$  and  $\varphi = 10^\circ$ , the radar cross section for different  $(\theta_s, \varphi_s)$  aspect angles is showed in Fig. 9. The peak response is given for  $(\theta_s = \theta, \varphi_s = -\varphi)$ .

Note that the backscattered field is very weak, so a dihedral can be hardly detected using monostatic configuration. Only dihedrals which are in the same direction than radar motion ( $\varphi_s = \varphi = 0^\circ$ ) can be detected.

## C. Ogive-Shaped Target Imaging

Now, the GTD-based models are used to characterize a circular ogive (see Fig. 10). This kind of object was already used in

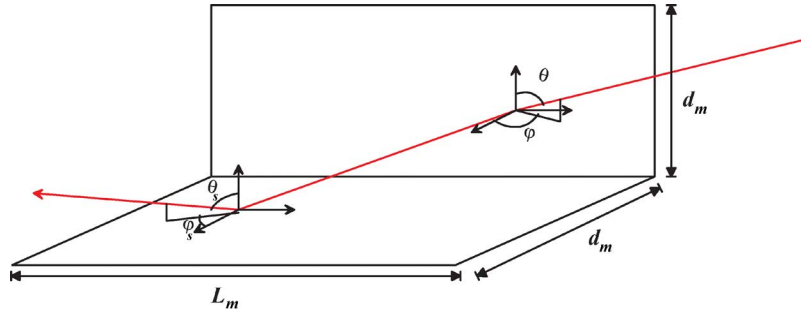


Fig. 8. Geometrical characteristics of electromagnetic field propagation for a  $L_m$  length and  $h_m$  height dihedral.

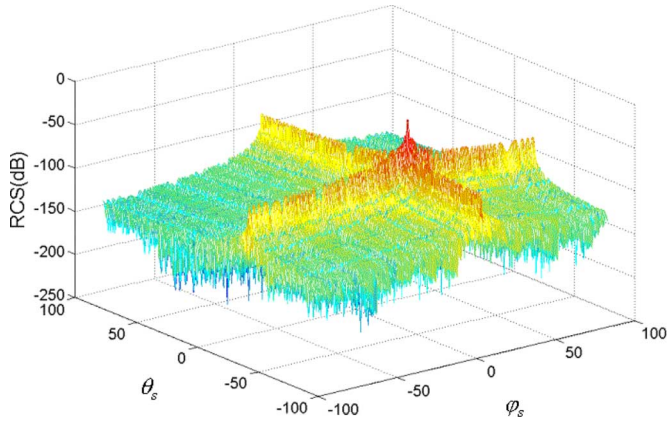


Fig. 9.  $(\theta_s, \phi_s)$  aspect angle bistatic RCS of a 10 m length and 5 m height dihedral.

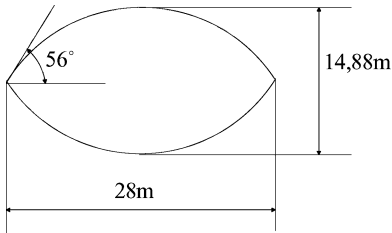


Fig. 10. Ogive characteristics.

[4] for a comparison between monostatic and bistatic radar images with an other model. In the present paper, a different configuration is considered but the proposed results are comparable.

The considered ogive is 28 m long and  $56^\circ$  angle as shown in Fig. 10. The frequencies ranging transmitted signal is [1.475, 1.525] GHz. With these parameters, the target is considered very large to the wavelength. So, using GTD-based models, the ogive could be assimilated to two infinite cones on its extremities and an infinite tangent plane on its sides.

Some simulations are realized in monostatic and bistatic configurations in order to compare image characteristics. In the monostatic configuration the radar move along the  $Y$ -axis from  $(-1000, 50, 0)$  m to  $(-1000, -50, 0)$  m so the aperture is 100 m (see Fig. 11). In the bistatic configuration, the transmitter is the same as in the monostatic case and the receiver move along the  $X$ -axis from  $(-25, -1000, 0)$  m to  $(25, -1000, 0)$  m. From these considerations the bistatic angle is  $90^\circ$  (see Fig. 11).

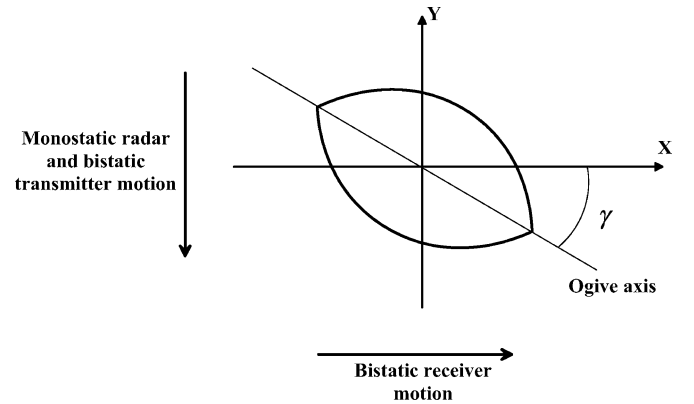


Fig. 11. Ogive imaging setup for the monostatic and the bistatic configurations.

In the first simulation (see Fig. 12) the ogive-axis is parallel to the  $X$ -axis ( $\psi = 0^\circ$ ). In the monostatic configuration, the obtained image shows relatively weak scattering ( $-23$  dB) from the tips. For the bistatic image, a stronger scattering center can be seen ( $-5$  dB). Also two weak scattering ( $-30$  dB) appear from the tips. For the considered low-observable target, these simulations illustrate the importance of considering bistatic scattering mechanisms from the point of view of the receiver.

In the second simulation (see Fig. 13), the ogive-axis and the  $X$ -axis make an angle  $\psi = 45^\circ$ . The monostatic and the bistatic images show different specular reflection positions. Both images present a strong scattering center but at different positions and there is an extra scattering center (the stronger one) in the bistatic image.

These results highlight that the acquisition configurations for both the monostatic and the bistatic cases have a strong influence on the obtained results. Moreover, the bistatic case seems more useful for target detection since it is able to bring information about the target (and so it is able to detect the target) even if planar surfaces are not normal to the look direction. Of course the receiver must also be positioned so that it can receive the scattered field.

#### D. Bistatic Radar Imaging of a (Simplified) Plane

In this part a more realistic complex target is considered. The object under test is a civil plane [see Fig. 14(a)]. It is made of



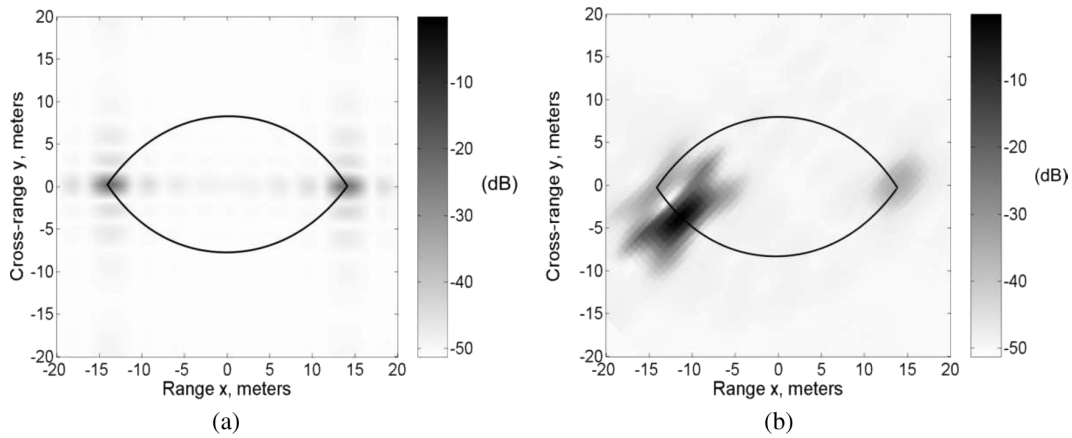


Fig. 12. Ogive-shaped target images. The ogive-axis is parallel to the  $X$ -axis ( $\psi = 0^\circ$ ). (a) monostatic image. (b) bistatic image.

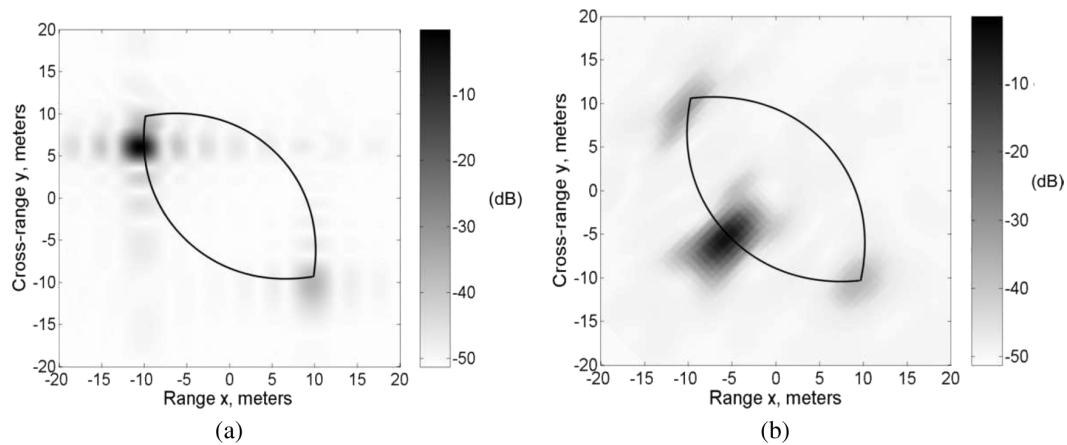


Fig. 13. Ogive-shaped target imaging for  $\psi = 45^\circ$ . Obtained image in (a) the monostatic configuration and (b) the bistatic configuration.

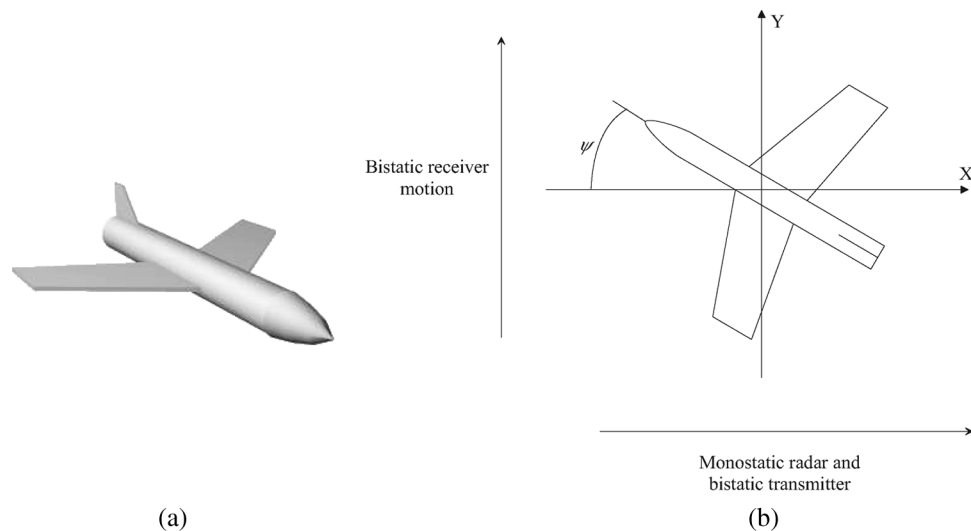


Fig. 14. (a) three-dimensional representation of the modeled plane. (b) definition of the orientation ( $\psi$ ) of the plane.

a cylinder for the fuselage, the mid part of an ogive stand for the nose, and the wing and the fin are made of finite strips, discontinuities and isotropic highlights. For this target the masking effects are taken into account.

The sizes of the plane are given in Fig. 15. For both the monostatic and the bistatic configurations, the transmitter is situated

at  $(0, -2000, 0)$ m. The aperture is 100 m, the central frequency is 2 GHz and the bandwidth is 80 MHz.

For this target two acquisitions are proposed depending on the angle  $\psi$  between the  $x$ -axis and the fuselage [see Fig. 14(b)]. Like for the previous target, the obtained monostatic images are different to the bistatic ones (see Figs. 16 and 17). These results

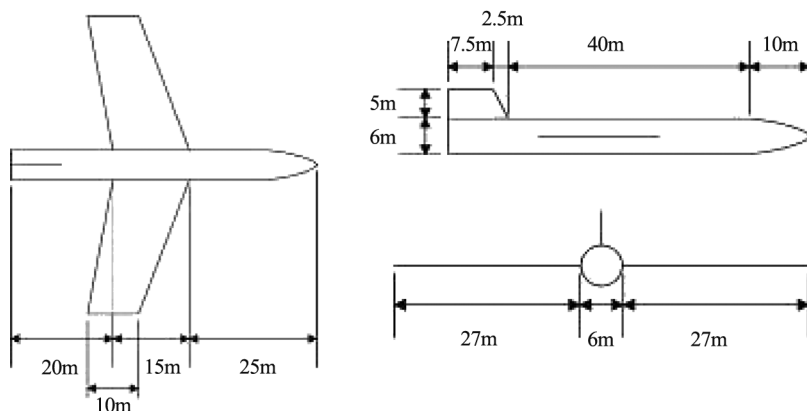


Fig. 15. Characteristics of the considered complex target: a civil plane.

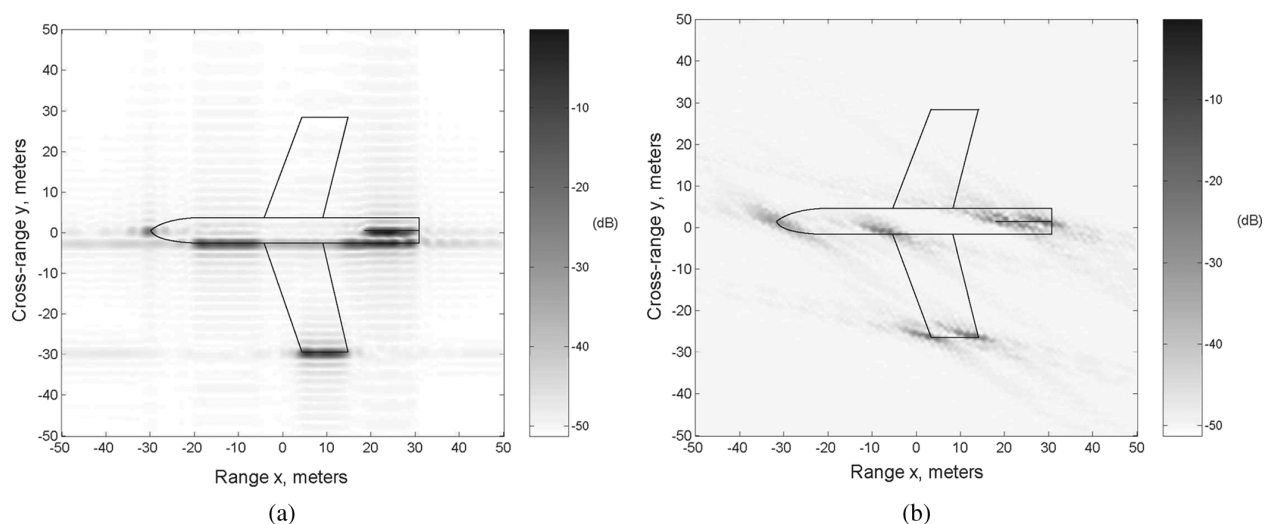


Fig. 16. Images obtained for the (simplified) plane from (a) the monostatic and (b) the bistatic configuration when  $\psi = 0^\circ$ .

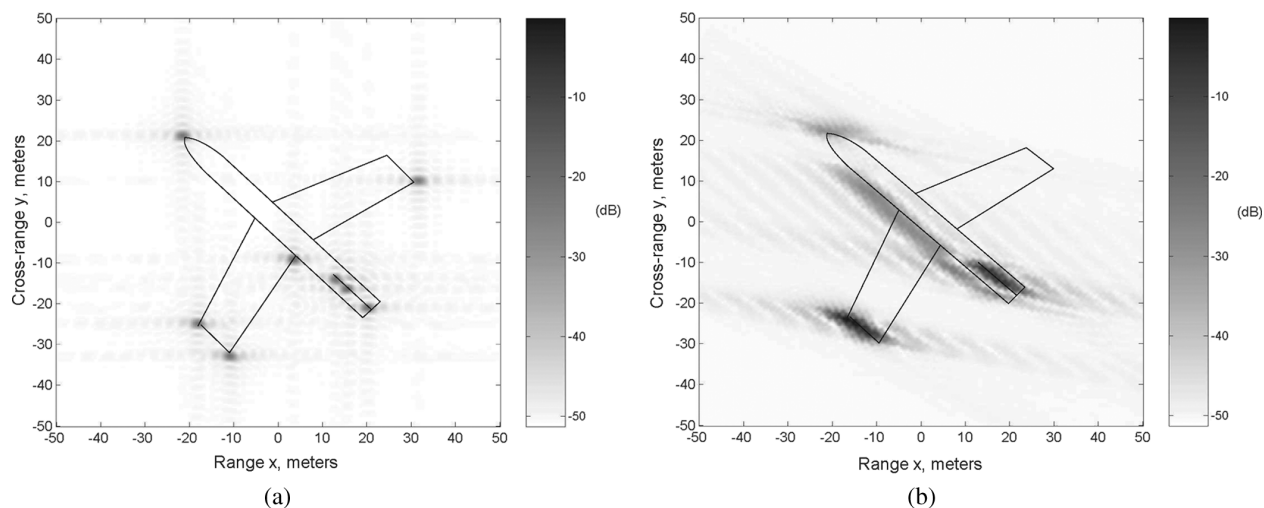


Fig. 17. Images obtained for the (simplified) plane from (a) the monostatic and (b) the bistatic configuration when  $\psi = 45^\circ$ .

also highlight the different scattering mechanisms observed in both configuration.

From these results and for future works, one can questioning which configuration is much more appropriate for target detection and classification. If bistatic configurations are able to ob-

tain specular returns from surfaces not normal to the look direction (in contrast with the monostatic one), they are also more complex and difficult to implement. However their ability to increase information about observed targets or general scenes cannot be neglected.

## V. CONCLUSION

This article presents a three-dimensional “full-polarized” bistatic model which take into account each component of the radar radiolink where the transmitter and the receiver are separated and are moving. The used signal received by a polarimetric bistatic radar is expressed as the voltage detected on the receiving antenna by taking into account the polarimetric behaviour of the target, and the mobile velocity effect. A bistatic SAR processing based on the monostatic range doppler algorithm has been developed without configuration restriction (moving transmitter, target and receiver) contrary to other previous works [3], [18].

The model and the obtained images are qualitatively compared with the well-known Soumekh’s codes and quantitatively from the given general analytical resolution equations. In the bistatic configuration, image resolutions are worst than in the monostatic one. But, the bistatic configuration cost is less expensive than the monostatic one (one transmitter, multi-receiver), so it is possible to make several acquisitions and enhance the bistatic resolution by data fusion.

Finally, GTD-based models are used in order to image complex targets in monostatic and bistatic configurations. In the monostatic case, only planar surfaces normal to the look direction give specular returns. This restriction can be break in a bistatic configuration. The considered simulations confirm this point and show the interest of bistatic and multistatic data acquisitions since they lead to get different information about the considered scene. However, bistatic systems are more complex to implement but the possible increase of information about the observed scene made them still attractive.

Also note that the developed model is a versatile tool permitting the simulation of a wide range of radar scenarios for various configurations (monostatic and bistatic) and various kinds of targets. It can be used to detect moving targets on the ocean surface including ships and ship wakes.

Then, our further researches could be focused on bistatic polarimetric capabilities for automatically target classification and recognition. One can also be interesting into bistatic imaging of sea surface for surface characterization, oil-spill or target and ship detection.

## ACKNOWLEDGMENT

The authors wishes to acknowledge M. Soumekh who gave them permission to introduce and use Fig. 3(a) from [17] in this paper.

## REFERENCES

- [1] O. Airiau and A. Khenchaf, “A methodology for modeling and simulating target echoes with a moving polarimetric bistatic radar,” *Radio Sci.*, vol. 35, no. 3, pp. 773–782, 2000.
- [2] N. Akhter, “Far zone electromagnetic scattering from complex shapes using geometrical theory of diffraction,” Ph.D. dissertation, Ohio State Univ., Columbus, 1993.
- [3] M. J. Ben Kassem, A. Khenchaf, and J. Saillard, “BISAR mapping modelization and processing,” in *Eur. Conf. on Propagation and Systems*, Brest, France, Mar. 15–18, 2005.
- [4] R. J. Burkholder, I. G. Gupta, and J. T. Johnson, “Comparison of monostatic and bistatic radar images,” *IEEE Antennas Propag. Mag.*, vol. 45, no. 3, pp. 41–50, 2003.

- [5] R. L. Eigel, P. J. Collins, A. T. Terzuoli, G. Nesti, and J. Fortuny, “Bistatic scattering characterization of complex objects,” *IEEE Trans. Geosci. Remote Sensing*, vol. 38, no. 5, pp. 2078–2092, 2000.
- [6] L. B. Felsen, “Plane-wave scattering by small-angle cones,” *IEEE Trans. Antennas Propag.*, vol. 5, no. 1, pp. 121–129, 1957.
- [7] J. I. Glaser, “Some results in bistatic radar cross section (RCS) of complex objects,” *Proc. IEEE*, vol. 77, no. 5, pp. 639–648, May 1989.
- [8] H. D. Griffiths, “Bistatic and multistatic radar,” in *Inst. Elect. Eng. Military Radar Seminar*, Shrivenham, U.K., Sep. 17, 2004.
- [9] L. Gurel, H. Bagci, J. C. Castelli, A. Cheraly, and F. Tardivel, “Validation through comparison: measurement and calculation of the bistatic radar cross section (BRCS) of a stealth target,” *Radio Sci.*, vol. 38, no. 3, pp. 12.1–12.10, 2003.
- [10] J. Homer, B. Mojarrabi, J. Palmer, K. Kubik, and E. Donskoi, “Non-cooperative bistatic SAR imaging system: spacial resolution analysis,” in *Proc. Int. Geoscience and Remote Sensing Symp. (IGARSS)*, Toulouse, France, Jul. 2003, pp. 1446–1449.
- [11] J. B. Keller, “Geometrical theory of diffraction,” *J. Opt. Soc. Amer.*, vol. 52, no. 2, pp. 116–130, 1962.
- [12] C. K. Ong, “Bistatic radar system,” Ph.D. dissertation, Univ. Queensland, Brisbane, Australia, Mar. 2003.
- [13] O. Loffeld, H. Nies, V. Peters, and S. Knedlik, “Models and useful relations for bistatic SAR processing,” *IEEE Trans. Geosci. Remote Sensing*, vol. 42, no. 10, pp. 2031–2038, 2004.
- [14] B. D. Rigling and R. L. Moses, “GTD-based scattering models for bistatic SAR,” in *Proc. SPIE*, G. Zelnio and F. D. Garber, Eds., Sep. 2004, vol. 5427, Algorithms for Synthetic Aperture Radar Imagerie XI, pp. 208–219.
- [15] G. T. Ruck, D. E. Barrick, W. D. Stuart, and C. K. Kirchbaum, *Radar Cross Section Handbook*. New York: Plenum Press, 1970.
- [16] M. Soumekh, *Synthetic Aperture Radar Signal Processing*. New York: Wiley-Interscience, 1999.
- [17] —, “Wide-bandwidth continuous-wave monostatic/bistatic synthetic aperture radar imaging,” in *Proc. Int. Conf. Image Processing (ICIP)*, Chicago, IL, Oct. 1998, pp. 361–365.
- [18] —, “Bistatic synthetic aperture radar inversion with application in dynamic object imaging,” *IEEE Trans. Signal Processing*, vol. 39, no. 9, pp. 2044–2055, 1991.
- [19] T. Zeng, M. Cherniakov, and T. Long, “Generalized approach to resolution analysis in BSAR,” *IEEE Trans. Aerospace Electron. Syst.*, vol. 41, no. 2, pp. 461–474, 2005.



**Fabrice Comblet** was born in 1979 in France. He received the master degree in automatic and industrial computer from the Université Scientifique et Technologique de Lille, France, and the Ph.D. degree from the Université de Bretagne Occidentale, Brest, France, in 2002 and 2005, respectively.

Since 2002, he has been with the E<sup>3</sup>I<sup>2</sup> Laboratory (EA3876)-ENSIETA, Brest, working on bistatic SAR.



**Ali Khenchaf** (M’93) received the Master Degree in statistical data processing from the University of Rennes I, France and the Ph.D. degree in electronic systems and computer network from the University of Nantes, Nantes, France, in 1989 and 1992, respectively.

From 1989 to 1993, he was a Researcher at the IRCCyN (UMR CNRS 6597) Laboratory, Nantes. His teaching courses are in the fields of numerical mathematics, electromagnetic wave propagation, waves and microwave, signal processing and operational research theory. From 1993 to 2001, he held an Assistant Professor position at the same university. In September 2001, he joined ENSIETA, Brest, France, where he is now a Professor and the Head of Laboratory E<sup>3</sup>I<sup>2</sup>-EA3876. He has published and presented many scientific contributions. His research interests include radar waves scattering, microwave remote sensing, electromagnetic wave propagation, scattering in random media, bistatic scattering of electromagnetic waves and target parameters estimation.



**Alexandre Baussard** received the Ph.D. degree from the Ecole Normale Supérieure, Cachan, France, in 2003.

From 2003 to 2004, he was a CNRS Postdoctoral Researcher at the L2S Laboratory. He is currently a Maître de Conférences at the Université de Bretagne Occidentale, Brest, France, working with the  $E^3I^2$  Laboratory-ENSIETA, France. His research deals with electromagnetic imaging, inverse problems, multiscale/multiresolution signal and image processing.

**Fabrice Pellen** is with the LSOL Laboratory (EA938), Brest, France.